Suspended Microchannel resonators with integrated electrodes for thermal and electrical characterization of liquids

Martín-Pérez *et al.*
Micro and Nano Systems Letters (2025) 13:12
https://doi.org/10.1186/s40486-025-00233-5

Micro and Nano Systems Letters

CORRESPONDENCE Open Access

Suspended Microchannel resonators with integrated electrodes for thermal and electrical characterization of liquids

Alberto Martín-Pérez[1*], Stefano Stassi[1] and Carlo Ricciardi[1*]

Abstract

Suspended microchannel resonator (SMR) has been demonstrated as a versatile technique, allowing to measure mechanical, morphological or even optical properties of cells. However, physical properties of cells may substantially change depending on the chemical composition of the suspension medium. Therefore, it is essential developing novel multiparametric techniques able to provide a complete understanding of the biological samples by characterizing also the liquid in which the cells are suspended. In this work we both theoretically and experimentally introduce a novel electro-mechanical sensing technique using SMR devices with integrated electrodes that allow measuring different physicochemical properties of the liquid sample as thermal conductivity, dielectric constant, electrical conductivity or even concentration of ions. These measured liquid properties can ultimately be used to complement other typical SMR measurements, such as mass. Moreover, we show that this electro-mechanical approach can be also used as a transduction method and as a way of tuning the mechanical resonance frequency.

Keywords Microfluidic devices, Nanomechanical sensors, Electrical sensors, Thermal properties, Electrical properties, Heat transfer, Electrolytes

Introduction

The next advances in biomedicine and biotechnology call for the development of innovative sensing techniques that allow us to reach an unprecedented comprehension of the biological entities. However, in many cases, monitoring only one parameter provides a limited knowledge of the biological system given that cells (as well as other biological entities) are not only in a continuous process of change but they can also present a wide variability among specimens from the same type. Physical parameters as cell size, density or mass not only change according to the phase of the cell life cycle, but also depends on the cell line [1, 2]. For this reason, the development of different techniques and platforms that allow the simultaneous acquisition of multiple parameters, both physical and chemical, of individual cells is gaining more and more relevance in the recent years.

In this context, the development of platforms for multiplexed physical sensing of individual cells has attracted the interest of the scientific community using a rich variety of approaches, such as microfluidics [3], nanomechanics [4] or optics [5]. In this scope, it became especially interesting the suspended microchannel resonator (SMR) sensing technique [6–10], which has been revealed as a highly versatile tool allowing to merge the three previously mentioned approaches in a single device. This technique consists on a device containing a microfluidic channel which, in a certain region (suspended area), is free-standing so it can oscillate in flexural mechanical modes. The advantage of maintaining the target analyte in a liquid environment, combined with the high

*Correspondence:
Alberto Martín-Pérez
alberto.martin@polito.it
Carlo Ricciardi
carlo.ricciardi@polito.it
[1] Department of Applied Science and Technologies (DISAT), Politecnico Di Torino, Corso Duca Degli Abruzzi 24, 10129 Turin, Italy

throughput and hydrodynamic forces provided by microfluidics, is further enhanced by extremely sensitive nanomechanical analysis. This analysis detects variations in mass or force within the suspended channel by measuring shifts in its mechanical resonance frequency. Thanks to this combination of approaches in a single device, this SMR technique has been proved as an interesting platform for the multiparametric sensing, having demonstrated not only its capability for performing individual cell mass sensing [11, 12], but also its capability of measuring other parameters of interest in biosensing such as growth rate [13], density [14, 15], compressibility [16] or hydrodynamic and hydrostatic forces [17–19]. Moreover, the SMR device unleashes its full potential when it is fabricated in an optically transparent material, allowing the optical imaging of the analytes [20] or the measurement of optical properties [21]. On the other hand, in parallel to this development of the SMR devices, different electrical techniques have been introduced using microfluidic channels for the passive control of cells and particles by the application of electric fields that allow trapping or separating particles [22, 23] or even techniques for characterization of physical properties of cells as the electric impedance spectroscopy [24]. Nevertheless, despite the high versatility of SMR devices or of the microchannels with integrated electrodes performing cell analysis, this investigation becomes more challenging if we consider that the different cell parameters may change depending on the physicochemical properties of the suspension medium [25]. Indeed, cell analysis should not be only limited to measure cell properties, but the physical and chemical properties of the cell buffer should be also measured, given these properties—in particular ion concentrations—have a significant effect on the measured cell properties. In this aspect, despite SMRs have been demonstrated to measure different physical properties which directly depend on the composition of the carrier liquid (as density [7, 8, 10], compressibility [18], refractive index [21] or heat capacity [26–28]), these properties do not allow by themselves elucidating directly the chemical composition of the medium.

In this work, we both theoretically and experimentally propose a novel electro-mechanical sensing approach to complement well-established measurements of cell physical properties (as mass, size or density) in SMR devices, with the relevant information on the physical and chemical composition of the carrier liquid. This technique enables the measurement of a liquid's thermal conductivity, as well as electrical properties such as permittivity and conductivity. Moreover, we demonstrate that the measurement of the electrical conductivity can be used for evaluating the concentration of ions in the solution present in the channel. Finally, we show that the developed electro-mechanical method can be also used as an actuation mechanism for the SMR device, as well as a way for tuning its mechanical frequency. Despite a complete disentanglement of thermal and electrical properties of tested solutions was not achieved here, this innovative approach paves the way for advanced multi-parameter sensing in SMR devices, with potential applications in chemical and biological analysis, environmental monitoring, and lab-on-a-chip technologies.

Experimental setup

In this work wed use a transparent suspended microchannel resonator device with two gold electrodes integrated on the suspended area fabricated by Femtoprint SA (Switzerland). This device consists of a doubly-clamped beam with an embedded microchannel through which a fluid can be flown, while on the top of the beam are placed the electrodes. Please note that the electrodes are not in direct contact with the inner of the channel (further details on the structure and dimensions of the device can be found in the section S.1. of the Supplementary Information). The electrodes are separated by a gap of 20 μm in the centre of the suspended beam, so when a voltage difference is applied between them, an electric field is obtained inside the suspended area (including the embedded microchannel), opening the door to work with the device not only as a mechanical resonator with an integrated microfluidic channel, but using it also as an electric capacitor. To fabricate these devices, we start from a silica glass wafer on which an optical lithography is employed to pattern the negative shape of the electrodes (Fig. 1a). After that, a 200 nm thick Ti/Au film is deposited. The next step consists on lifting off the resin, obtaining the gold electrodes and then exposing the wafer to a femtosecond laser. The parts exposed to the laser suffer physicochemical changes (compared to their unexposed counterparts) and will be etched when the wafer is introduced in a potassium hydroxide solution. This laser-assisted etching results especially convenient to fabricate these suspended microchannels since the exposure can be done in different focal planes, allowing the release of a suspended beam with buried microchannels, along with a network of buried and surface microchannels that enable liquid introduction into the device (further details can be found in the section S.1. of the Supplementary Information). Finally, the device is sealed with a PDMS layer by means of an oxygen plasma treatment (Fig. 1a). Further details on the fabrication process can be found in our previous work [8].

Once the SMR device is prepared, it is mounted under a laser doppler vibrometer (MSA-500, Polytec, Germany) for its mechanical characterization (Fig. 1b). The output signal of the vibrometer is connected to the

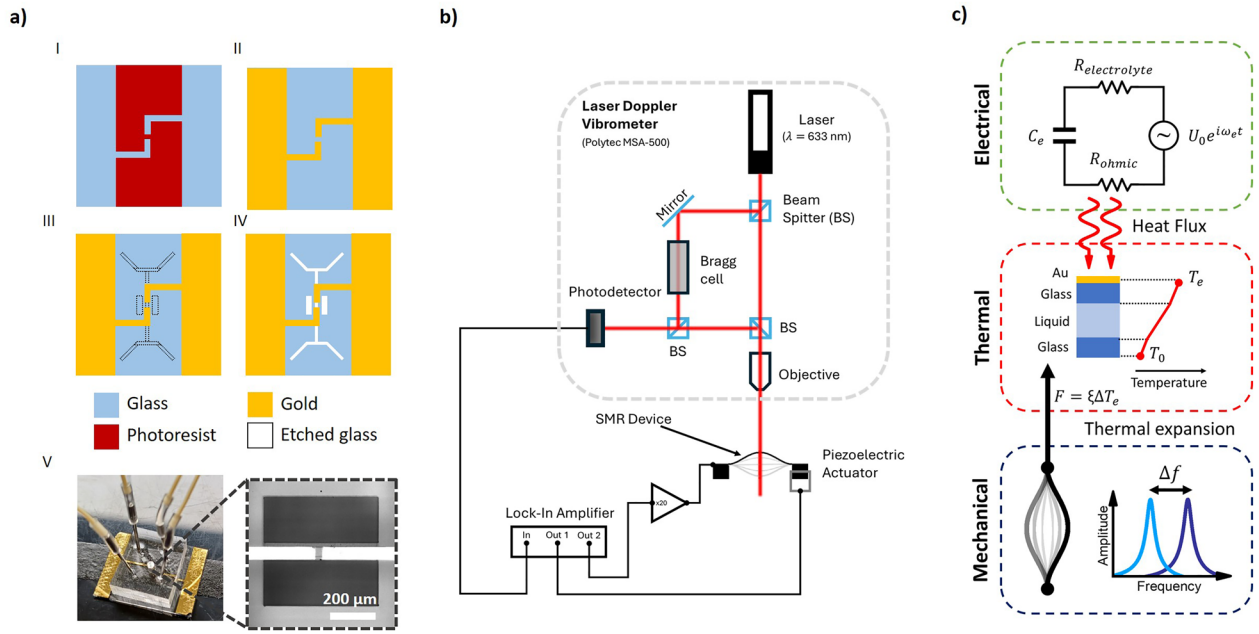

Fig. 1 Experimental setup and analytical model. **a** Steps of the fabrication process. I. Photolithography. II. Gold deposition and lift-off. III. Exposure to femtosecond laser. IV. KOH wet etching. V. Photography of the finished device sealed with the PDMS. Inset: microscope image of the suspended region of the SMR device with integrated electrodes. **b** Schematic of the experimental setup. **c** Schematic showing how the electrical, thermal and mechanical parts of the device interact among each other. Please note that if the inner liquid is not an electrolyte $R_{electrolyte} = 0$

input of a lock-in amplifier (UHFLI2, Zürich Instruments, Switzerland), in order to track the device oscillation while actuated with a piezoelectric transducer (PZT), controlled by the output signal of the lock-in amplifier. The piezoelectric transducer is attached to the SMR device, so when a voltage difference is applied between its extremes, a vibration is transmitted to the SMR inducing the motion of the suspended microchannel. Moreover, the electrodes of the SMR are connected to an additional output of the lock-in amplifier after passing through a constant-gain high-voltage amplifier (A400, Pendulum Instruments, Sweden), so AC voltages can be applied to the electrodes with amplitudes up to 200 V (peak voltage). No sign of electromigration or corrosion in the electrodes was evident from optical images, even after prolonged measurements.

On the other hand, the microfluidic inlets and outlets located in the PDMS layer of the SMR device are connected by means of flexible tubes to a microfluidic gas pressure pump (MFCS-EZ, Fluigent, France). This pump allows obtaining a Poiseuille flow inside the channels by controlling the pressure difference among the different inlets and outlets. Moreover, the use of this microfluidic pump allows changing in a controlled manner the liquid inside the suspended region.

Analytical model and working principle

The proposed device combines three different techniques: nanomechanical sensor, microfluidic device and electric circuit. This hybrid approach opens the door to the emergence of multiphysical phenomena that can be used to develop a multiparameter sensor. Hereinafter we investigate how the application of an electrical voltage to the SMR electrodes varies the mechanical properties of the device (Fig. 1c).

Electrically, this SMR device can be modelled as a resistor–capacitor (RC) circuit given the intrinsic ohmic resistance of the gold electrodes as well as the electrical capacity obtained by the gap between the electrodes (Fig. 1c). Consequently, when a voltage is applied, the resistive heating by Joule effect eventually produces a thermal expansion of the electrodes (Eq. 1) that introduces a mechanical stress in the resonator (Eq. 2). The combination of these phenomena induces a variation of different mechanical properties of the device when a voltage is applied. The impedance of the device combining an ohmic resistance and a capacitor, makes the electrical-induced mechanical properties variations not only depend on the thermal properties of the inner liquid (as done in previous works using purely ohmic impedances [26, 27]), but also makes them depend on the electrical properties of the fluid.

$$\frac{dx}{x_0} = \alpha \Delta T \tag{1}$$

$$\sigma = E\alpha \Delta T \tag{2}$$

Being $\frac{dx}{x_0}$ the strain produced by the thermal expansion, α the linear thermal expansion coefficient, ΔT the temperature variation (compared to the room temperature), σ the induced mechanical stress and E the Young's Modulus.

Given the geometrical constrictions of the device, we can assume this stress to be introduced only in the direction of the axis of the device. This uniaxial stress will introduce a mechanical tension (F) in the resonator which eventually changes the dynamics of the resonator. This mechanical tension is directly proportional to the temperature difference in the electrode (ΔT_e) and to the tension susceptibility (ξ, a parameter that depends on structural factors of the device), as shown in Eq. 3. Please see Supplementary Information (section S.2.) for a complete derivation of the tension and the tension susceptibility parameter.

$$F = \xi \Delta T_e \tag{3}$$

To know the temperature in the electrodes, it is first necessary calculating the dissipated power in the electrodes. To this purpose, we consider a sinusoidal voltage and obtain the value of the dissipated power as the real part of the product of the current intensity and the voltage drop over the extremes of the equivalent circuit (Eq. 4).

$$P_{joule}(t) = {U_0}^2 R_e \frac{(C_e\omega_e)^2}{1 + (R_c C_e \omega_e)^2} \sin^2(\omega_e t)\cos(\varphi_e) \tag{4}$$

Being P_{joule} the dissipated power, U_0 the amplitude of the applied voltage, R_e the intrinsic ohmic resistance of the electrodes, C_e the electrical capacity, ω_e the angular frequency applied in the electrode, R_c the total resistance of the circuit and φ_e the electrical phase (given as $\arctan[R_c C_e \omega_e]^{-1}$). Initially we are going to consider the resistance of the electrodes as the unique resistance contribution (i.e. $R_e = R_c$), while when filling the device with electrolytes, an additional variable resistance will be computed.

Having an expression for the dissipated power we can now use this value to calculate the temperature in the electrode (T_e), which will govern the changes in the resonance frequency of the device. Consequently, the dissipation of this heat will determine the temperature of the system. Given the characteristics of the device, we can do some assumptions that will make easier the calculation of this temperature distribution. Firstly, since we expect small temperature variations ($\Delta T/T_0 \ll 1$), we can neglect radiation-based heat transfer, while we can also neglect convective heat transfer since we expect the same temperature at both extremes of the microchannel. Secondly, given that the electrodes are much larger than both the suspended region and the device width, we can simplify the model by assuming that heat flux is unidirectional and does not flow along the axial direction. The electrode geometry favours heat transfer primarily toward the opposite face of the electrodes. The validity of this unidirectional heat flux assumption was checked with three-dimensional finite element simulations (further details can be found in Supplementary Information, S.3.). Thirdly, for the sake of simplicity, we can assume a quasi-static model so that the temperature responses immediately to the changes in the power. Moreover, despite the device is made by three layers of different materials (glass/liquid/glass) we will study it as homogeneous and isotropic with a constant effective thermal conductivity. This effective conductivity results from averaging the thermal conductivities of the different materials weighed to their respective thicknesses. Finally, we impose as boundary conditions the temperature in the extreme (the one without the gold electrodes) at room temperature (T_0), while the other extreme has the temperature of the gold electrodes (T_e). Please note that, since the thickness of the gold electrodes is two orders of magnitude lower than the thicknesses of the glass and the liquid, we can reduce them in this model to a point temperature. Having made all these considerations, the temperature of the electrodes can be determined by the balance between the heat flux provided by Joule heating and the heat flux evacuated to the room by conduction (Eq. 5).

$$\frac{dQ}{dt} = P_{joule}(t) - \frac{\kappa_{eff} A_e}{W}[T_e(t) - T_0] \tag{5}$$

Being dQ the heat variation, κ_{eff} the effective thermal conductivity of the device, A_e the area of the electrodes, W the width of the device and T_0 the room temperature.

Considering that the temperature variation is directly proportional to the heat variation, being heat capacity (C_h) the proportionality constant, a differential equation is obtained (Eq. 6), which can be solved by the Fourier method, thus achieving the temperature of the electrodes as a function of time (Eq. 7).

$$\frac{dT_e}{dt} = \frac{1}{C_h}\left[P_{joule}(t) - \frac{\kappa_{eff} A_e}{W}[T_e(t) - T_0]\right] \tag{6}$$

$$T_e = T_0 + \frac{\sqrt{2\pi}}{2}(C_e U_0)^2 R_e \cos(\varphi_e)\left(\frac{W}{\kappa_{eff} A_e}\right)\frac{{\omega_e}^2}{1+(R_c C_e \omega_e)^2}\left(1+\frac{\cos(2\omega_e t-\varphi_t)}{\sqrt{1+\left(\frac{2C_h W \omega_e}{\kappa_{eff} A_e}\right)^2}}\right) \quad (7)$$

Being $\varphi_t = \arctan\left(\frac{\kappa_{eff} A_e}{2\omega_e C_h W}\right)$.

From Eq. 7 it can be appreciated that the temperature in the electrodes is composed by the sum of a static and a time-dependent term, being the static term the average value of temperature, while the time-dependent term introduces a periodical variation over this value.

Experimental verification of the model

In this section we apply the previously proposed analytical model to evaluate how the voltage applied to the electrodes can change different aspects of the nanomechanical motion (oscillation amplitude and resonance frequency) of the SMR device and finally compare these theoretical predictions with experimental results. We here demonstrate that the electrodes can be used to actuate the mechanical oscillations, as well as they can be implemented to tune the mechanical resonance frequency of the SMR device. Additionally, studying how the applied voltage affects the resonance frequency sets the bases for the analysis of the electrical and thermal properties of the inner liquid that will be done in the following sections.

Effect of the applied voltage in oscillation amplitude

From the time dependent term in the temperature equation (Eq. 7), it can be deduced that this electrical heating can be used to induce the oscillation of the SMR device, therefore opening the possibility of using the electrodes as actuators for the SMR device. The temperature variation, through thermal dilatation effect, produces a periodic displacement in the gap between the electrodes (also the center of the suspended area) that will introduce a force (Eq. 3) parallel to the axis of the SMR in each electrode. Despite these two forces have the same magnitude and opposite direction, in the center of the gap there will be a deformation due to Poisson effect, producing the displacement of the mechanical resonator (Fig. 2a, Eq. 8).

Being z the displacement along the orthogonal direction respect to the resonator axis, ν the Poisson ratio and A_{cs} the area of the cross section. Please note the static term of the temperature has been dismissed since it does not produce any oscillation.

To check the validity of the proposed model, we evaluate this displacement by measuring the mechanical spectra of the SMR while applying an alternate voltage to the electrodes. Moreover, to have a comparison for this method, we also measure the same flexural modes using the piezoelectric transducer as actuator. In the case of the actuation with the electrodes on the clamped–clamped beam, the oscillation frequency (demodulation frequency in the lock-in amplifier) should be the double of the applied frequency (output frequency in the lock in amplifier), given the effect of the factor $2\omega_e$ inside the cosine in Eq. 8.

Looking at Fig. 2, it can be appreciated that the 1st and the 3rd flexural modes obtained using the electrodes as actuation method reproduce the results obtained with piezoelectric actuator, but with an amplitude three orders of magnitude lower (Fig. 2b, d). On the other hand, the 2nd flexural mode was found to be measurable only using the piezoceramic actuation (Fig. 2c). This is consistent with the proposed model in which the force applied by the electrodes is located in the middle of the beam, thus given the node at this point for this specific mode the actuation becomes ineffective.

Either in the case of the actuation with the piezoceramic or with the electrodes, the mode shape was measured as the profile of the oscillation amplitude as a function of the axial position. In the case of the 1st and the 3rd flexural modes (Fig. 2b, d) the mode shapes are consistent with the mode shapes obtained by the Euler–Bernoulli model. The mode shapes obtained with the electrode transduction are noisier than those obtained

$$z(t) = -\frac{\sqrt{2\pi}}{2}\frac{\nu x_0 \xi}{A_{cs} E}(C_e U_0)^2\left(\frac{W}{\kappa_{eff} A_e}\right)\frac{R_e \cos(\varphi_e){\omega_e}^2}{1+(R_c C_e \omega_e)^2}\frac{\cos(2\omega_e t-\varphi_t)}{\sqrt{1+\left(\frac{2C_h W \omega_e}{\kappa_{eff} A_e}\right)^2}} \quad (8)$$

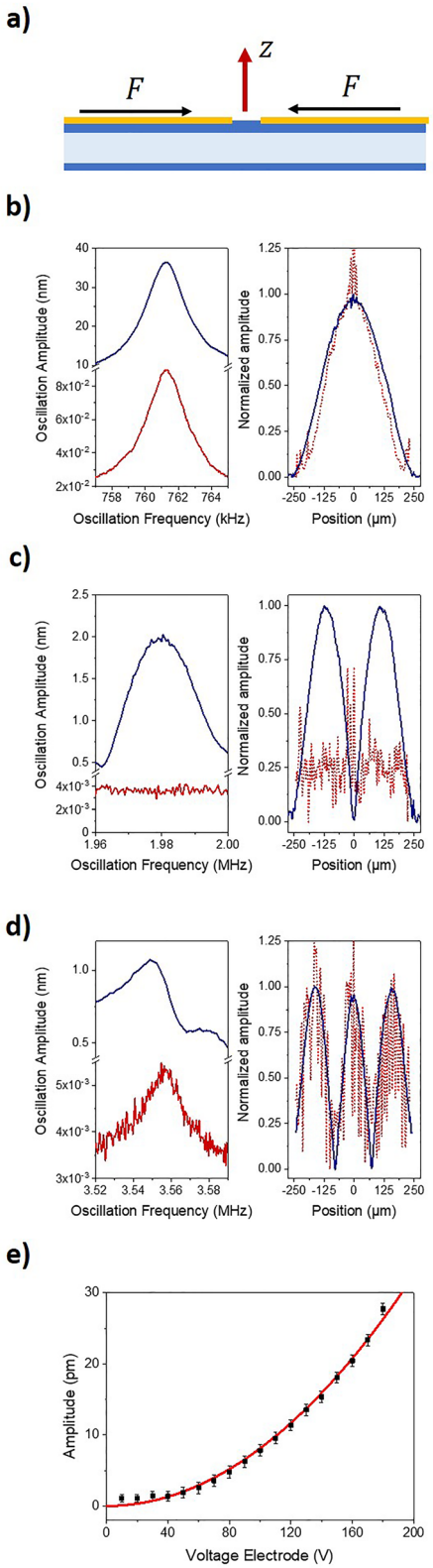

◀ **Fig. 2** Effect of the electrodes on the oscillation amplitude. **a** Schematic of the stress and the forces acting on the SMR device while applying a voltage signal to the electrodes. Comparison of the mechanical spectrum (left) and mode shape (right) measured actuating the SMR device with the piezoelectric transducer (blue line) and using the electrodes (red line) for the first (**b**), second (**c**) and third (**d**) flexural modes. **e** Amplitude of the first flexural mode as a function of the applied voltage to the electrodes and its fit to a parabola (red line)

with the piezoelectric actuator, which can be attributed to the weaker signal obtained when exciting with the electrodes. To compare in a quantitative manner the noise level between both transduction modes, we measured the frequency stability of the 1st flexural mode finding minimum noise level at 0.05 Hz for the piezoelectric actuator while this value is > 1 Hz for the electrode actuation (see section S.4. in Supplementary Information for further details). Nevertheless, despite the higher noise presented by the electrodes as actuation methods, they are revealed as an interesting method when used at higher modes (Fig. 2d). More specifically, in the measurements of the 3rd mode (Fig. 2d), it can be seen how the mechanical spectrum obtained with the piezoelectric actuator is distorted and does not fit well to the Lorentzian-like shape of the mechanical resonance. This distortion can be attributed to a bad transmission of the acoustic waves generated by the piezoceramic device at high frequencies. On the opposite, actuating with the electrodes we obtain a mechanical spectrum of the 3rd flexural mode without this distortion.

Additionally, we also measured how the oscillation amplitude in the acquired spectra changes with the amplitude of the applied voltage. For this purpose, we evaluate the oscillation amplitude at the resonance frequency by fitting the different spectra to a Lorentzian function. The obtained results (Fig. 2e) show a quadratic trend for this oscillation amplitude as a function of applied voltage, which agrees with the analytical model (Eq. 8).

The results obtained for the mechanical actuation of the SMR device using the electrodes demonstrate that, in general terms, it is not an efficient method when compared to an external piezoelectric actuator. For this reason, hereinafter, a piezoelectric disk will be employed as actuator. Nevertheless, using the electrodes as mechanical actuator has provided valuable inputs for checking the validity of the model.

Electrical modulation of the resonance frequency

Another effect arising from the mechanical stress introduced by applying a voltage to the gold electrodes is a fine tuning of the resonance frequency. To study this tuning,

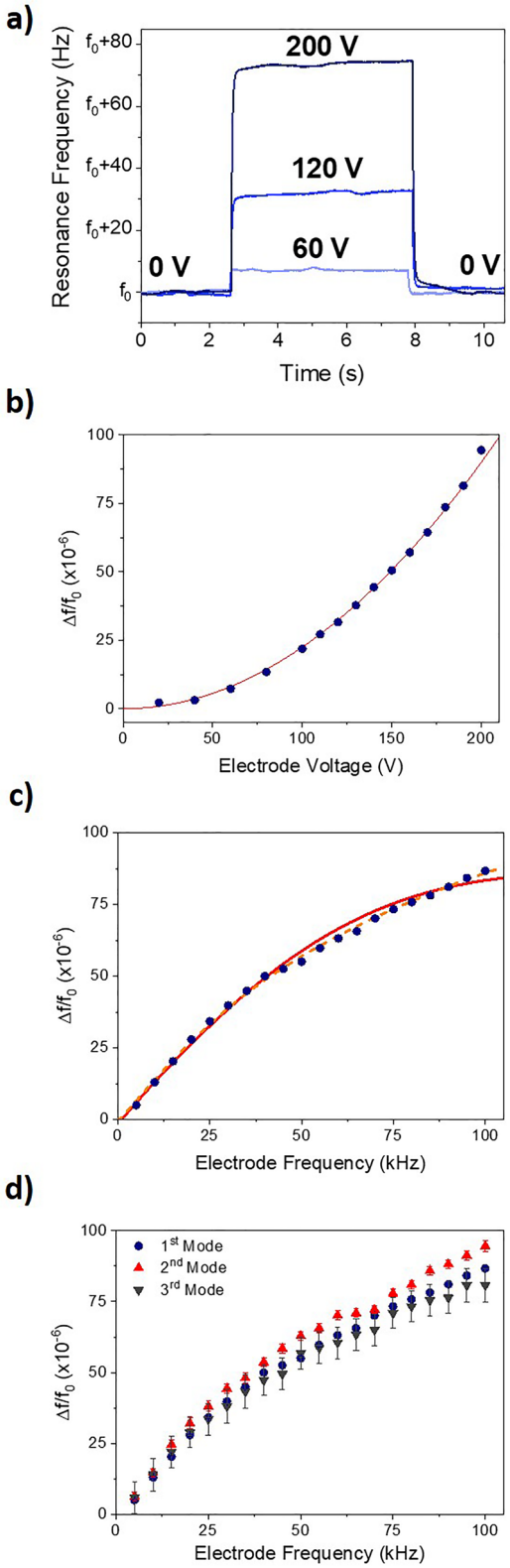

◀ **Fig. 3** Effect of the electrical actuation on the mechanical resonance frequency. **a** Mechanical resonance frequency measured when the electrodes are switched off/on/off with different voltages and a constant actuation frequency of 100 kHz. **b** Frequency shift measured as a function of the applied voltage for a fixed electrode frequency of 100 kHz (blue points) and its fit to a parabola (red solid lines). **c** Frequency shift measured as a function of the applied frequency in the electrodes for a fixed voltage of 200 V (blue points) and their fits to the model curve (red solid lines) and the model curve considering second-order effects (orange dashed line). **d** Frequency shift as a function of the applied frequency for the first three flexural modes

we consider the SMR as a vibrating string whose tension is modulated by the heating (Eq. 3). Therefore, the relative frequency shift can be calculated as this tension increment divided by twice the initial tension (F_0). For the calculation of this relative frequency shift (Eq. 9), we consider the average value of the stress variation since we have not resolution in the experimental setup to measure the periodical changes of the stress over the time.

$$\frac{\Delta f}{f_0} = \frac{\sqrt{2\pi}}{4F_0A_e}\xi W U_0^2 \left(\frac{C_e^2}{\kappa_{eff}}\right) \frac{R_e \cos(\varphi_e)\omega_e^2}{1+(R_cC_e\omega_e)^2} \tag{9}$$

Being Δf the resonance frequency shift and f_0 the resonance frequency when no voltage is applied.

We measured this effect using the piezoelectric actuator to excite the motion of the SMR device and tracking its mechanical resonance frequency in real time. When we switch on and off the voltage in the electrodes we register an immediate shift in the resonance frequency as a consequence of the mechanical tension introduced by the voltage (Fig. 3a).

Given the dependence of the mechanical frequency shift with different experimental parameters (Eq. 9), we can obtain response curves of the frequency shift as a function of different experimental parameters such as the applied voltage, frequency, thermal conductivity or electrical capacity. Consequently, we can use this response curves not only to check the validity of the analytical model, but also for sensing purposes (as will be shown in the next sections). When we study how the applied voltage affects the mechanical resonance frequency (using a constant applied frequency of 100 kHz), we find a growing parabolic trend (Fig. 3b), which is in good agreement with the analytical model (Eq. 9). On the other hand, varying the applied frequency (keeping a constant voltage of 200 V) we find that the mechanical resonance frequency is increased with the applied frequency (Fig. 3c). To check the validity of the model, we made a non-linear fit of these experimental data to the function in Eq. 9 (solid red line in Fig. 3c). In this case, despite obtaining a high a coefficient of determination in this fitting (0.975)

it becomes evident that there is a second-order discrepancy between the model and the experimental data. Nevertheless, when introducing second order corrections to the fitting function (equation S.8, orange dashed line in Fig. 3c), a match between data and the fitting is observed, increasing the coefficient of determination up to 0.998 (see Supplementary Information, S.5., for further details).

Moreover, additional experiments were carried out to check the validity of the proposed model. On one hand, we repeat the measurements of the response curves for higher modes (second and third flexural modes) obtaining no significant differences between the relative frequency shift dependence for the different modes (Fig. 3d). This fact is consistent with the string approach proposed. On the other hand, we also studied how the frequency shift is affected by applying different flow rates of the liquid, finding the frequency shift is reduced as the flow rate is increased. This finding is compatible with the proposed electrothermal cause of the frequency shift, since the applied flow introduces a new source of heat dissipation, reducing the electrodes temperature (see Supplementary Information, S.6., for further details). Nevertheless, for a better understanding on this effect it is necessary introducing a term to consider a forced convection in Eq. 6, something that goes beyond of the scope of this paper. Please note that any other measurement presented in this work was done without applying a flow.

Characterizing physical properties of liquids

Until this point, all the experiments showed were performed with the SMR device filled with deionized water. However, the microfluidic system connected to SMR allows changing easily the inner liquid, so different physical properties can be easily tuned by introducing solutions with different concentrations, opening the door to exploit the dependence of the electrical frequency tuning (Eq. 9) on parameters such as the thermal conductivity or electrical permittivity. Firstly, when the inner liquid is changed, a shift in the mechanical resonance frequency proportional to the density difference is registered. The variation of the mass of the liquid inside the suspended channel allows the device to work as a density sensor with a responsivity of − 0.44 mL/μg and a limit of detection of 2 μg/mL (see Supplementary Information for further details), which is within the range of the state of the art of similar SMR sensors [7, 8, 10, 18]. Given the density differences between the used solutions, in the experiments presented hereinafter, for each solution the relative frequency shifts will be referred to the resonance frequency measured initially for each specific solution without any alteration (f_0).

Nevertheless, when we apply a voltage to the SMR filled with different liquids, the proposed device is revealed as a powerful tool for measuring different physical properties of liquids, since the response curve (Eq. 9) change with parameters as the electrical capacity, as well as its thermal conductivity. Please note that the electric capacity is proportional to the electrical permittivity of the inner liquid and, for aqueous solutions, it changes linearly with the electrical permittivity (see Supplementary Information, S.8., for further details on this aspect). If one of these two parameters is changed while keeping the other constant, we can straightforwardly model how the resonance frequency shift is affected by this variation (compared to a reference solution, Eqs. 10 and 12) defining a thermal conductivity and an electrical permittivity responsivity for our device (Eqs. 11 and 13), respectively. Moreover, if the thermal conductivity and the permittivity change simultaneously, the frequency shift can be obtained as the product of Eqs. 10 and 12.

$$\left(\frac{\Delta f}{f_0}\right)_{liq} = \left(\frac{\Delta f}{f_0}\right)_{ref} \left(\frac{1}{1+\mathcal{R}_{th}\Delta\kappa_{liq}}\right) \tag{10}$$

$$\mathcal{R}_{th} = \left(\frac{2W_{wall}}{W_{liq}}\kappa_{wall} + \kappa_0\right)^{-1} \tag{11}$$

$$\left(\frac{\Delta f}{f_0}\right)_{liq} = \left(\frac{\Delta f}{f_0}\right)_{ref} (1+\mathcal{R}_{\varepsilon}\Delta\varepsilon)^2 \tag{12}$$

$$\mathcal{R}_{\varepsilon} = \frac{C_1}{C_0 + C_1\varepsilon_{ref}} \tag{13}$$

Being $\left(\Delta f/f_0\right)_{liq}$ the frequency shift of each specific liquid, $\left(\Delta f/f_0\right)_{ref}$ the frequency shift produced by a liquid taken as reference, $\mathcal{R}_{th}$ the responsivity to thermal conductivity variations, W_{wall} the thickness of the wall of the SMR device, W_{liq} the thickness of the inner channel, κ_{wall} the thermal conductivity of the walls of the SMR device, κ_0 the thermal conductivity reference liquid, $\mathcal{R}_{\varepsilon}$ the responsivity to electrical permittivity changes, C_0 and C_1 the fitting parameters for the electric capacity as a function of the permittivity (see Supplementary Information, S.8. for further details).

To check the validity of the proposed device as thermal and electrical properties sensor, we varied progressively the characteristics of the inner liquid by introducing aqueous solution of glycerol with different concentrations ranging from 0 to 14% (in weight). Measuring the response curves of the relative resonance frequency deviation using different glycerol solutions (Fig. 4a), it can be seen that the shift increases with the concentration of

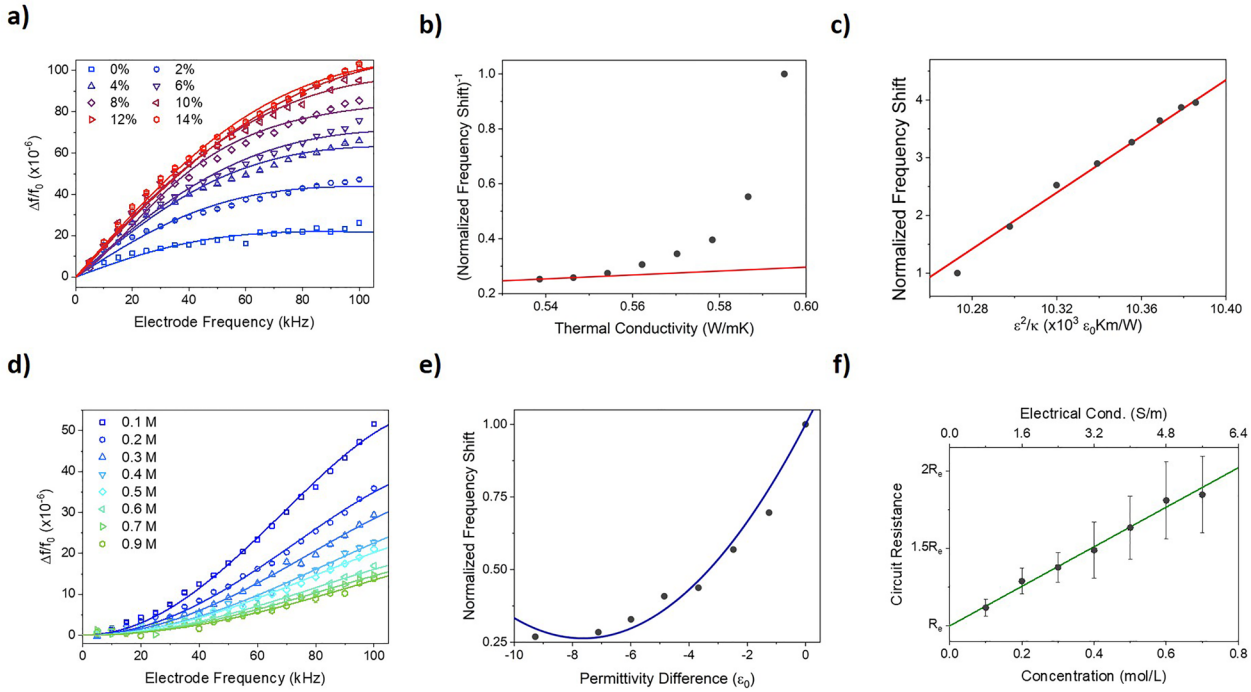

Fig. 4 Multiparametric physicochemical characterization. **a** Response curve measured for the device filled with aqueous solutions of glycerol with different concentrations (dots) and its fit to the analytical model (solid lines). **b** Response measured of the device for a given voltage (200 V) and applied frequency (100 kHz) as a function of the thermal conductivity (dots) and a tangent to this curve (solid line). The normalized frequency shift shown hereinafter in the vertical axis is the relative frequency shift of each liquid divided by the relative frequency shift of the reference liquid (pure water). **c** Response measured for a given voltage (200 V) and applied frequency (100 kHz) as a function of the quotient of the square of the electrical permittivity and the thermal conductivity (dots) and its linear fit (solid line). **d** Response curve measured for the device filled with aqueous sodium chloride solutions with different concentrations (dots) and its fit to the analytical model (solid lines). **e** Response measured of the device for a given voltage (200 V) and applied frequency (100 kHz) as a function of electrical permittivity (dots) and its fit to a parabola (solid line). **f** Calibration plot for the device resistance as a function of the electrical conductivity and the ionic concentration

glycerol. This trend in the response curves indicates that the effect of the reduction on the thermal conductivity due to the glycerol concentration (from 0.59 WK^{-1} m^{-1} at 0% concentration to 0.54 WK^{-1} m^{-1} at 14% concentration, known from the nominal values) dominates over the reduction in the electrical permittivity (from 78 ε_0 at 0% concentration to 74 ε_0 at 14% concentration, also known from the nominal values). However, when plotting the inverse of the frequency shift for a specific voltage (200 V) and applied frequency (100 kHz) as a function of just the thermal conductivity of the liquid (Fig. 4b), we do not obtain a linear trend as the model predicts (Eq. 10). However, the curve in Fig. 4b tends to a linear behavior for low thermal conductivities (i.e. high glycerol concentration), indicating that in this range the effect of neglecting the variations on the electrical permittivity is appropriate. Thus, we can extrapolate the responsivity to the thermal conductivity in such a region as the tangent of the curve, obtaining a responsivity of 0.7 km/W, which is in a good agreement with the expected value from the analytical model ($\sim$ 1 km/W). On the contrary, if we plot the frequency shift as a function of the quotient of the square of the permittivity and the thermal conductivity, a linear trend is obtained (Fig. 4c). This result agrees with the analytical model and reveals that, despite in the chosen solutions the effect of the variation in thermal conductivity is higher than the effect of the variation in the electrical permittivity, the effect of the frequency variation induced by this last parameter cannot be neglected with the changes in concentration.

Alternatively, to demonstrate the use of the SMR device as an electrical permittivity sensor, we introduced sodium chloride aqueous solutions with different concentrations ranging from 0.1 to 0.9 M inside the microchannel. In this specific case, we can neglect the problem of the simultaneous variation of the thermal conductivity and the electrical permittivity since, given the concentration range used, the variation of the thermal conductivity is lower than 1%, while the electrical permittivity varies around 10% [29]. Please note that, despite the fact of keeping the thermal conductivity constant while the electrical permittivity is varying does not represent the general case,

the specific case of using sodium chloride is of high relevance when it comes to analyze samples of biological interest. Now, when plotting the response curves for the different concentrations (Fig. 4d) it is appreciated that the frequency shift becomes higher when the concentration decreases (i.e. when the permittivity increases). Moreover, when plotting the frequency shift for a constant applied frequency (100 kHz) and voltage (200 V) of the electrical stimulus given to the gold electrodes as a function of the permittivity (Fig. 4e), a quadratic trend is appreciated as predicted by the analytical model (Eq. 12). Additionally, from this fit it is obtained a responsivity of $0.013\ {\varepsilon_0}^{-1}$.

Nevertheless, the response curves in this case (Fig. 4d) present a different shape than those obtained with the glycerol solutions (Fig. 4a). This change in the curvature of the frequency shift response is due to the electrolytic nature of the NaCl solutions, turning our device into an electrolytic capacitor, which needs introducing some additional considerations in the equivalent electrical circuit. Sodium chloride introduces charge carriers in the inner liquid which shields the electrical field produced by voltage in the electrodes. Please note that a glass insulating layer separates the liquid from the electrodes. This shielding reduces the magnitude of the electric field, resulting in a lower current in the electrodes. Regarding the equivalent circuit (Fig. 1c), this shielding effect can be modelized as a new resistance connected in series to the capacitor, whose value is directly proportional to the ionic conductivity (Eq. 14), increasing the overall resistance of the circuit.

$$R_c = R_e + \gamma\,\lambda \tag{14}$$

Being γ an electric and geometric factor and λ the electrical conductivity of the electrolyte.

On the other hand, the response curve (Eq. 9) presents an inflection point, whose position depends on the resistance of the circuit, so the higher the circuit resistance, the higher the electrode actuation frequency at which this inflection point happens. For the measurements previously obtained with the dielectric glycerol-water solutions, this inflection point was positioned at a frequency lower than the frequency range used (from 5 to 100 kHz) however, thanks to the resistance increase produced by using an electrolyte, this inflection point is displaced to higher values and now it can be appreciated within the investigated electrode actuation frequency range, which explains the different curvature in these response curves.

As a consequence of this increase of the electrical resistance, the response curve can be simplified by approaching it to a polynomial function thanks to a Taylor expansion around ω_e=0 (Eq. 15).

$$\frac{\Delta f}{f_0} \approx R_e \cos(\varphi_e)\left({\omega_e}^2 - {C_e}^2 {R_c}^2 {\omega_e}^4\right) \tag{15}$$

This new version of the response curve not only makes easier the fitting of the experimental data, but also opens the door to quantify the value of the variations in the circuit resistance. From Eq. 15, it can be deduced that the value of the resistance of the circuit can be extracted by operating with the second (p_2) and fourth order (p_4) parameters obtained in the fitting of the response curves, as shown in Eq. 16. Moreover, given the dependency of the circuit resistance with the electrical conductivity (Eq. 14), we can use the device as a sensor of the electrical conductivity. Given that for the concentration range we used the electrical conductivity of NaCl is directly proportional to the concentration of ions, we can define a calibration plot for the ion concentration as follows:

$$\sqrt{\frac{p_4}{{p_2}^2}} = R_e + mM \tag{16}$$

Being M the molarity of the solution and m the conversion factor from conductivity to concentration.

Plotting the circuit resistance as a function of the electrical conductivity as well as the molarity (Fig. 4f), we obtain a linear response (as expected) revealing a 10.5 R_em/S responsivity in electrical conductivity and a 1.3 R_e/mol in concentration. Considering the initial estimation the electrodes ohmic resistance ($\sim 2\ \Omega$, see section S.8. in Supplementary Information for further details), these values became 21 m/S and 2.6 mol^{-1}.

Conclusions

In this work, we have both theoretically and experimentally introduced a novel method for using a suspended microchannel resonator as a multiparametric sensor, by integrating gold electrodes to form a capacitor in the centre of the SMR device. When a voltage is applied to the SMR device, the impedance of the electrodes dissipates a part of the electrical energy in thermal heating and, consequently, a mechanical stress is introduced in the resonator due to the thermal expansion of the electrodes. We have proved that this effect allows actuating the mechanical resonator as well as finely tuning its mechanical resonance frequency. However, while checking experimentally the actuation method using the electrodes helped to support the validity of the analytical model, it should be underline that this actuation method is not efficient as an external piezoelectric disk, given the highly noise signal it provides. The capacitor structure of the device makes the dissipated power and, consequently, the frequency shift depends either on the thermal conductivity or the electrical permittivity

of the inner liquid. We eventually exploited this feature of the tuning of the resonance frequency to develop a new approach for determining the thermal and electrical properties of the liquids. Finally, we have taken advantage of the induced electrical resistance that appears when the SMR is filled with an electrolyte to correlate it to the electrical conductivity and the ionic concentration of the solution. One of the challenges of this technique that should be addressed in future works is disentangling the dependence between the thermal conductivity and the electrical permittivity in the frequency shift response. In this work we have also indicated one possible path to develop this solution by introducing a flow in the internal channel that can modulate the heat dissipation.

Supplementary Information

The online version contains supplementary material available at https://doi.org/10.1186/s40486-025-00233-5.

Additional file 1.

Acknowledgements
This publication is part of the project NODES, which has received funding from the MUR–M4C2 1.5 of PNRR with grant agreement no. ECS00000036. This research has been cofounded by European Union—Next Generation EU Programme within the project P2022CBHZK (PRIN 2022 PNRR).

Author contributions
AM and CR conceived and designed the work. CR and SS designed the devices. AM developed the analytical model and performed the experiments. AM wrote the manuscript with inputs from all authors. All authors analyzed the data, discussed the results and commented on the manuscript.

Funding
This work was funded by the MUR—M4C2 1.5 of PNRR with grant agreement no. ECS00000036. This research has been cofounded by European Union—Next Generation EU Programme within the project P2022CBHZK (PRIN 2022 PNRR).

Availability of data and materials
The datasets used and/or analysed during the current study are available from the corresponding author on reasonable request.

Declarations

Competing interests
Carlo Ricciardi reports financial support was provided by Ministry of Education and Merit. If there are other authors, they declare that they have no known competing financial interests or personal relationships that could have appeared to influence the work reported in this paper.

Received: 10 June 2025 Accepted: 30 July 2025
Published online: 10 August 2025

References

1. Zlotek-Zlotkiewicz E, Monnier S, Cappello G, Le Berre M, Piel M (2015) Optical volume and mass measurements show that mammalian cells swell during mitosis. J Cell Biol 211:765–774. https://doi.org/10.1083/jcb.201505056
2. Son S et al (2015) Resonant microchannel volume and mass measurements show that suspended cells swell during mitosis. J Cell Biol 211:757–763. https://doi.org/10.1083/jcb.201505058
3. Chang Y-N et al (2019) Microfluidic analysis for separating and measuring the deformability of cancer cell subpopulations. ACS Omega 4:8318–8323. https://doi.org/10.1021/acsomega.8b02249
4. Malvar O et al (2016) Mass and stiffness spectrometry of nanoparticles and whole intact bacteria by multimode nanomechanical resonators. Nat Commun 7:13452. https://doi.org/10.1038/ncomms13452
5. Suzuki Y et al (2019) Label-free chemical imaging flow cytometry by high-speed multicolor stimulated Raman scattering. Proc Natl Acad Sci U S A 116:15842–15848. https://doi.org/10.1073/pnas.1902322116
6. Pastina AD, Maillard D, Villanueva LG (2018) Fabrication of suspended microchannel resonators with integrated piezoelectric transduction. Microelectron Eng 192:83–87. https://doi.org/10.1016/j.mee.2018.02.011
7. Lee D et al (2016) Pulled microcapillary tube resonators with electrical readout for mass sensing applications. Sci Rep 6:33799–33807. https://doi.org/10.1038/srep33799
8. Calmo R et al (2019) Monolithic glass suspended microchannel resonators for enhanced mass sensing of liquids. Sens Actuators B Chem 283:298–303. https://doi.org/10.1016/j.snb.2018.12.019
9. Burg TP, Manalis SR (2003) Suspended microchannel resonators for biomolecular detection. Appl Phys Lett 83:2698–2700. https://doi.org/10.1063/1.1611625
10. Malvar O et al (2015) Highly sensitive measurement of liquid density in air using suspended microcapillary resonators. Sensors (Basel, Switzerland) 15:7650–7657. https://doi.org/10.3390/s150407650
11. Burg TP et al (2007) Weighing of biomolecules, single cells and single nanoparticles in fluid. Nature 446:1066–1069. https://doi.org/10.1038/nature05741
12. Ko J et al (2019) In 20th international conference on solid-state sensors, actuators and microsystems & eurosensors XXXIII (TRANSDUCERS & EUROSENSORS XXXIII), pp 748–751.
13. Cetin AE et al (2017) Determining therapeutic susceptibility in multiple myeloma by single-cell mass accumulation. Nat Commun 8:1613–1624. https://doi.org/10.1038/s41467-017-01593-2
14. Grover WH et al (2011) Measuring single-cell density. Proc Natl Acad Sci U S A 108:10992–10996. https://doi.org/10.1073/pnas.1104651108
15. Martín-Pérez A et al (2021) Hydrodynamic assisted multiparametric particle spectrometry. Sci Rep 11:3535. https://doi.org/10.1038/s41598-021-82708-0
16. Kang JH et al (2019) Noninvasive monitoring of single-cell mechanics by acoustic scattering. Nat Methods 16:263–269. https://doi.org/10.1038/s41592-019-0326-x
17. Khan MF, Knowles B, Dennison CR, Ghoraishi MS, Thundat T (2014) Pressure modulated changes in resonance frequency of microchannel string resonators. Appl Phys Lett. https://doi.org/10.1063/1.4889744
18. Martín-Pérez A, Ramos D, Tamayo J, Calleja M (2021) Nanomechanical molecular mass sensing using suspended microchannel resonators. Sensors (Basel) 21:3337
19. Martín-Pérez A, Ramos D (2023) Nanomechanical hydrodynamic force sensing using suspended microfluidic channels. Microsyst Nanoeng 9:53. https://doi.org/10.1038/s41378-023-00531-1
20. Ko J, Lee D, Lee BJ, Kauh SK, Lee J (2019) Micropipette resonator enabling targeted aspiration and mass measurement of single particles and cells. ACS Sens 4:3275–3282. https://doi.org/10.1021/acssensors.9b01843
21. Martín-Pérez A et al (2019) Mechano-optical analysis of single cells with transparent microcapillary resonators. ACS Sens 4:3325–3332. https://doi.org/10.1021/acssensors.9b02038
22. Pesch GR et al (2018) Bridging the scales in high-throughput dielectrophoretic (bio-)particle separation in porous media. Sci Rep 8:10480. https://doi.org/10.1038/s41598-018-28735-w
23. Cardenas-Benitez B et al (2020) Direct current electrokinetic particle trapping in insulator-based microfluidics: theory and experiments. Anal Chem 92:12871–12879. https://doi.org/10.1021/acs.analchem.0c01303
24. Zou X, Spencer DC, Morgan H (2025) Single-cell impedance spectroscopy of nucleated cells. Lab Chip 25:2939–2948. https://doi.org/10.1039/D5LC00111K

25. Urbanska M et al (2020) A comparison of microfluidic methods for high-throughput cell deformability measurements. Nat Methods. https://doi.org/10.1038/s41592-020-0818-8
26. Ko J, Khan F, Nam Y, Lee BJ, Lee J (2022) Nanomechanical sensing using heater-integrated fluidic resonators. Nano Lett 22:7768–7775. https://doi.org/10.1021/acs.nanolett.2c01572
27. Ko J, Lee BJ, Lee J (2023) Advanced operation of heated fluidic resonators via mechanical and thermal loss reduction in vacuum. Microsyst Nanoeng 9:127. https://doi.org/10.1038/s41378-023-00575-3
28. Maillard D, De Pastina A, Abazari AM, Villanueva LG (2021) Avoiding transduction-induced heating in suspended microchannel resonators using piezoelectricity. Microsyst Nanoeng 7:34. https://doi.org/10.1038/s41378-021-00254-1
29. Ramires MLV, Nieto de Castro CA, Fareleira JMNA, Wakeham WA (1994) Thermal conductivity of aqueous sodium chloride solutions. J Chem Eng Data 39:186–190. https://doi.org/10.1021/je00013a053

Publisher's Note